

**Fe₂P@mesoporous carbon nanosheets synthesized via an organic template
method as a cathode electrocatalyst for Zn-air batteries**

Electrochemical Measurements: All the electrochemical measurements were conducted at room temperature in a three-electrode system with an electrochemical workstation (CHI 760E electrochemical workstation). In this work, the catalyst inks were prepared as follows: 4 mg of the CNSs, Pt/C (5%), RuO₂ catalysts by ultrasonically dispersing in 1.01 mL mixed solution contained 500 μL of deionized water, 500 μL of isopropyl alcohol and 10 μL of Nafion (5 wt%) solution. Then, the well-dispersed 10 μL of ink was pipetted onto the glassy carbon electrode as the working electrode and dried at room temperature. The amount of catalyst loading is 0.2 mg/cm² for all the samples. The electrolyte (0.1 M KOH solution) was purged with pure N₂ or O₂ for at least 30 min to obtain the N₂/O₂ saturated solution before the ORR tests. The Pt foil and Ag/AgCl ($E_{\text{RHE}} = E(\text{Ag}/\text{AgCl}) + 0.059 \cdot \text{pH} + 0.222 \text{V}$) were employed as the counter electrode and the reference electrode, respectively. The cyclic voltammograms (CVs) of different catalysts were performed in an N₂/O₂-saturated KOH solution at a scan rate of 50 mV/s. The RDE/RRDE tests were measured at varying rotating rates from 400 to 2025 rpm with a scan rate of 10 mV/s. The stability tests were measured by current versus time (i-t) chronoamperometric response at a constant potential of -0.4 V (vs. Ag/AgCl). The number of electrons transferred (n) at different electrode potentials was determined by the K-L Equations (J^{-1} vs $\omega^{-1/2}$) according to equation (1), (2):

$$1/J = 1/J_L + 1/J_K = 1/B\omega^{1/2} + 1/J_K \quad (1)$$

$$B = 0.2nFC_0D_0^{2/3}\nu^{-1/6} \quad (2)$$

where J is the measured current density, J_K and J_L are the kinetic and diffusion-limiting current densities, ω is the rotating speed of the electrode, n is the electron transfer number, F is the Faraday constant (96485 C/mol), C₀ is the bulk concentration of O₂ (1.2 × 10⁻³ mol/L for 0.1 M KOH solution), D₀ is the diffusion coefficient of O₂ (1.9 × 10⁻⁵ cm²/s for 0.1 M KOH solution), and ν is the kinematic viscosity of the electrolyte

(0.01 cm²/s for 0.1 M KOH solution). The constant 0.2 is employed if the rotation rate is expressed in rpm.

The RRDE was adopted for the measurement of the peroxide (H₂O₂) yields (%) and the electron transfer number (n) during the ORR process, which can be calculated by Equation (3) and (4):

$$\text{H}_2\text{O}_2 (\%) = (200 I_r/N) / (I_d + I_r/N) \quad (3)$$

$$n=4 I_d / (I_d + I_r/N) \quad (4)$$

where I_r is the ring current, I_d is the disk current, and the N is a constant of 0.37, representing the ring collection efficiency of the electrode.

The electrical double-layer capacitance (C_{dl}) of the catalysts were measured from double-layer charging curves using cyclic voltammograms (CVs) in a potential range of 0-0.2V vs Ag/AgCl. The plot of the current density against scan rate was collected at 0.1V, which shows a linear relationship, with its slope as the double-layer capacitance (C_{dl}).

Zn-Air Battery Test: The rechargeable Zn-air battery tests were performed in a two electrode battery under ambient conditions. The cathode was prepared by coating CNS-900 catalysts onto carbon paper and dried at 60 °C for 2 h (1.0 mg/cm²). The polished zinc sheets was used as the air electrodes. Both electrodes were assembled into a home-made Zn-air battery with 6 M KOH aqueous solution containing 0.2 M Zn(OAc)₂·6H₂O as the electrolyte. The battery testing was performed in room environment on a LAND CT2001A instrument. The cycling was carried out for 20 min or 1h cycles (10 min discharge/charge or 0.5h discharge/charge) at current density of 10 mA/cm² or 50 mA/cm², respectively.

Flexible solid-state Zn-air battery:

A polished zinc foil (0.10 mm thickness) was used as anode. The air electrode was made by dropping a certain volume of catalyst ink onto a cleaned carbon cloth substrate (0.5 × 2.0 cm²) with a catalyst loading of 1 mg/cm². The gel polymer electrolyte was prepared as follows: 1.0 g polyvinyl alcohol (PVA) powder (MW 19500, Aladdin) was dissolved in 10.0 mL deionized water at 95 °C under magnetic stirring for 4 h. Then 3

mL of 6 M KOH filled with 0.2 M Zn(Ac)₂ (dissolved in KOH to form zincate, Zn(OH)₄²⁻) was added and the electrolyte solution was kept stirring at 95 °C for 1h. Then the solution was freezed at -3 °C over 12 h, and then thawed at room temperature. The procedure was repeated twice to gelate the PVA robustly. PVA is flexible, bendable, and stretchable, delivering considerable ionic conductivity and mechanical flexibility for flexible Zn-air batteries (Figure S16). Then the flexible solid-state Zn-air battery was assembled with air electrode and zinc foil placed on the two sides of PVA gel.

DFT calculations details

To understand the experimental investigation, first-principles density functional theory (DFT) calculations were used in the Vienna ab initio simulation package (VASP) ^{1, 2} with projector-augmented wave (PAW) ^{3, 4} pseudo-potentials. The generalized gradient approximation (GGA)-type functional, parameterized by Perdew, Burke and Ernzerhof (PBE), ⁵ was implemented to describe electron exchange and correlation energy. The plane-wave cutoff energy for the wave function was set to 400 eV. All structures were considered relaxed until the total energy was converged to 10⁻⁵ eV and all atomic forces were smaller than 0.05 eV Å⁻¹. Spin-polarized calculations have been performed. The electronic structure of the catalyst has been analyzed by partial density of state (PDOS) and charge transfers were derived from the Bader charge analysis.^{6, 7}

A single-layer periodical (5 × 5) supercell was built with the double defects of 48 carbon atoms. Then four N atoms substituted four C atoms, a Fe atom was anchored at the N atoms site of the graphene (namely, FeN₄). And two neighbor N atoms in FeN₄ model were substituted by two P atoms, denoted as FeN₂P₂. The vacuum layer between sheet was >20 Å, which was sufficiently large to avoid the periodic effect between slabs. In addition, the 4 layer-thick Pt (111) surface was built, respectively. The vacuum layer between slabs was >15 Å, which was sufficiently large to avoid the periodic effect between slabs. The phase molecules were simulated using a cubic cell of 15 Å × 15 Å × 15 Å³, in which the Brillouin zone integration was treated for the Γ point only. The averaged adsorption energies (E_{ads}) were calculated using the expression:

$$E_{\text{ads}} = E_{\text{adsorbate+surface}} - E_{\text{adsorbate}} - E_{\text{surface}}$$

Where $E_{\text{adsorbate+surface}}$, $E_{\text{adsorbate}}$, E_{surface} is the total energy of surface attached with adsorbate, the energy of adsorbate, and the energy of clean surface. By this definition, the more-negative energy indicates that the adsorbate is easier to be covered into surface.

The structural information of MCNS-900, CB and CMF

In this study, N, P-codoped carbon nanosheets embedding Fe_2P were facilely prepared from layered organic hybrids with melamine and pig blood. Doped nitrogen species originated from the melamine and doped phosphorus species came from the pig blood. Further, the Fe_2P nanoparticles were formed in situ under carbonization process without further phosphating. To investigate the role of **Fe_2P nanoparticles** on the electro-catalysis, the CNS-900 samples was further ground by ball-milling for 2 h to destroy the carbon shells around the Fe_2P nanoparticles. After the milling step, the catalyst was soaked in 1 M H_2SO_4 for 12 h to remove the Fe_2P nanoparticles and the resulting sample was denoted as MCNS-900. To investigate the role of **N doping** on the electro-catalysis, the pig blood powder without melamine was hydrothermally treated under the same condition as CNS-900. The resulting product was directly carbonized at 900 °C for 2 h and the sample was marked as CB. To investigate the role of **P doping** on the electro-catalysis, the melamine and FeCl_3 were hydrothermally treated under the same condition. The resulting product was directly carbonized at 900 °C for 2 h and the sample was marked as CMF.

To elucidate the elementary compositions and crystal diffractions, XPS and XRD measurements were conducted on MCNS-900. Figure S15a, b showed that the total Fe and P signals of MCNS-900 became weaker comparing to these of CNS-900 after the ball-milling and acid leaching step. For the MCNS-900 sample, there was no detectable diffraction peak of the iron species (Figure S15d). Figure S15c showed that the total N signal of MCNS-900 was similar to these of CNS-900. Pyridinic nitrogen and graphitic nitrogen were the dominant types of nitrogen in the MCNS-900 sample, accounting for 34.2% and 31.2% of the total nitrogen. The Fe-N of MCNS-900 accounting for 12.8%

of the total nitrogen, which decreased slightly on account for the removal of Fe₂P nanoparticles (Table S2). The XPS and XRD results clearly demonstrated that most of the Fe₂P nanoparticles have been removed and most of Fe-N was maintained in the MCNS-900 after the ball-milling and acid leaching step. The TEM images of MCNS-900 (Figure S16a, b) further confirmed that few Fe₂P nanoparticles were observed after the ball-milling and acid leaching step.

XPS and XRD measurements were also conducted on CB sample. Figure S15a, b showed that the Fe and P elements existed in CB sample. A series of small peaks at $2\theta = 40.3^\circ$, 44.2° and 47.3° were appear in the XRD pattern of CB sample, which were assigned to the (111), (201) and (210) reflections of the Fe₂P (JCPDS card no. 51-0943). The TEM images (Figure S16c, d) further confirmed that the Fe₂P nanoparticles existed in CB sample. Figure S15c showed that the total N signal of CB was negligible comparing to these of CNS-900 and MCNS-900. Moreover, graphitic nitrogen was the dominant type of nitrogen accounting for 50.1% of the total nitrogen and Fe-N was inappreciable in the CB sample. The XPS and XRD results clearly demonstrated that the CB sample contained Fe₂P nanoparticles and few Fe-N.

XPS and XRD measurements were also conducted on CMF sample. Figure S15a and S17b showed that the Fe and N elements were exist into CMF sample. Figure S15b showed that the total P signal of CMF was negligible comparing to these of CNS-900, CB and MCNS-900. A series of small peaks at $2\theta = 43.7^\circ$, 57.5° and 69.2° were appear in the XRD pattern of CMF sample, which were assigned to the (111), (112) and (300) reflections of the Fe₃N (JCPDS card no. 49-1663). Moreover, two peaks at $2\theta = 44.7^\circ$, and 65.0° were also appear in the XRD pattern of CMF sample, which were assigned to the (110) and (200) reflections of the Fe (JCPDS card no. 06-0696) (Figure S17 a). The SEM images (Figure S16 e, f) further confirmed that the Fe₃N and Fe nanoparticles were exist into CMF sample. Pyridinic nitrogen and pyrrolic nitrogen were the dominant types of nitrogen in the CMF sample, accounting for 34.6% and 20.8% of the total nitrogen. The Fe-N of CMF accounting for 13.9% of the total nitrogen, which was similar to that of MCNS-900 (Table S2).



Figure S1 SEM images of melamine (a) before hydrothermal process and (b, c) after hydrothermal process; the insets are digital photograph respectively

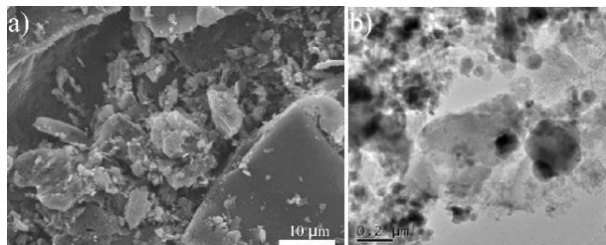


Figure S2 (a) SEM image of CMB; (b) TEM image of CB

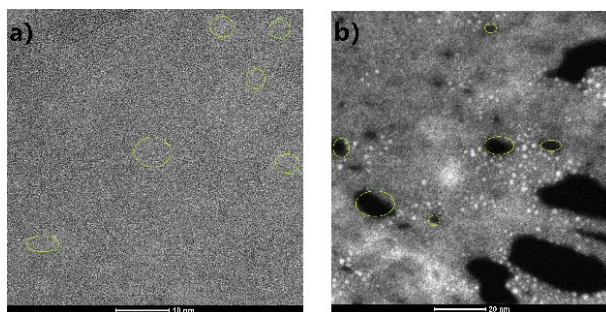


Figure S3 (a) HRTEM image and (b) HAADF-STEM images of carbonization sample; the green cycles indicated mesopores

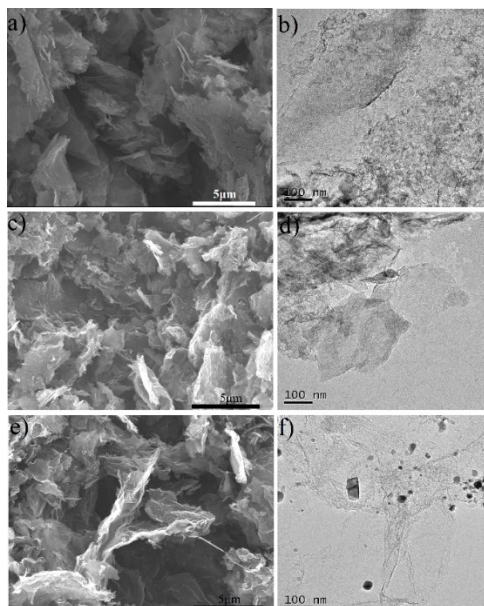


Figure S4 (a, c, e) SEM images of CNS-700, 800, 1000; (b, d, f) TEM images of CNS-700, 800, 1000

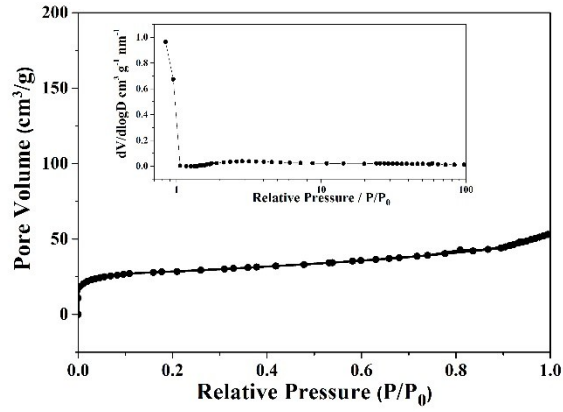


Figure S5 N₂ adsorption isotherms and pore size distributions of CB

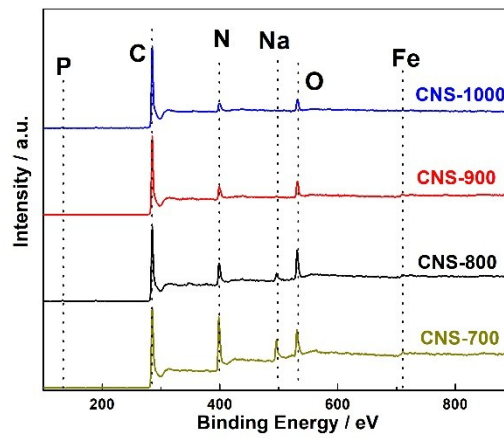


Figure S6 XPS spectra of CNS-700, 800, 900, 1000

The XPS peak at 497 eV ascribing to Na Auger appears for CNS-700 and CNS-800. The Na derived from blood powder can be maintained without water washing, when the carbonization temperature was below boiling point of sodium (883°C). With increasing carbonization temperature to above boiling point of sodium, the peak at 497 eV disappear for CNS-900 and CNS-1000.

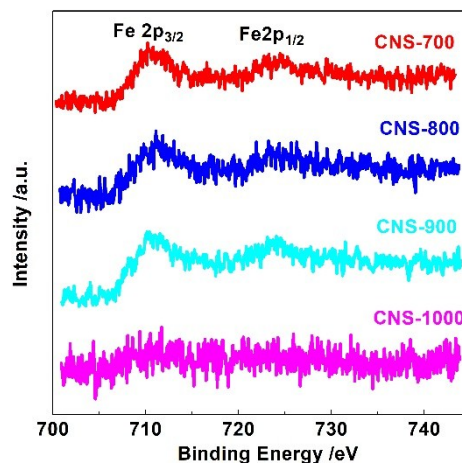


Figure S7 XPS high-resolution spectra of Fe 2p for CNS-700, 800, 900, 1000

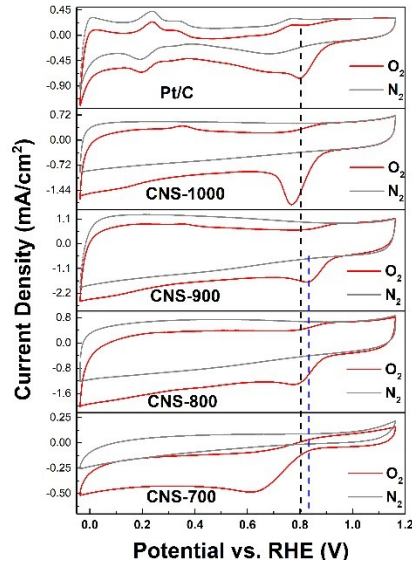


Figure S8 CV curves of CNS samples and Pt/C in N_2 and O_2 -saturated 0.1 M KOH solution at scan rate of 50 mV/s

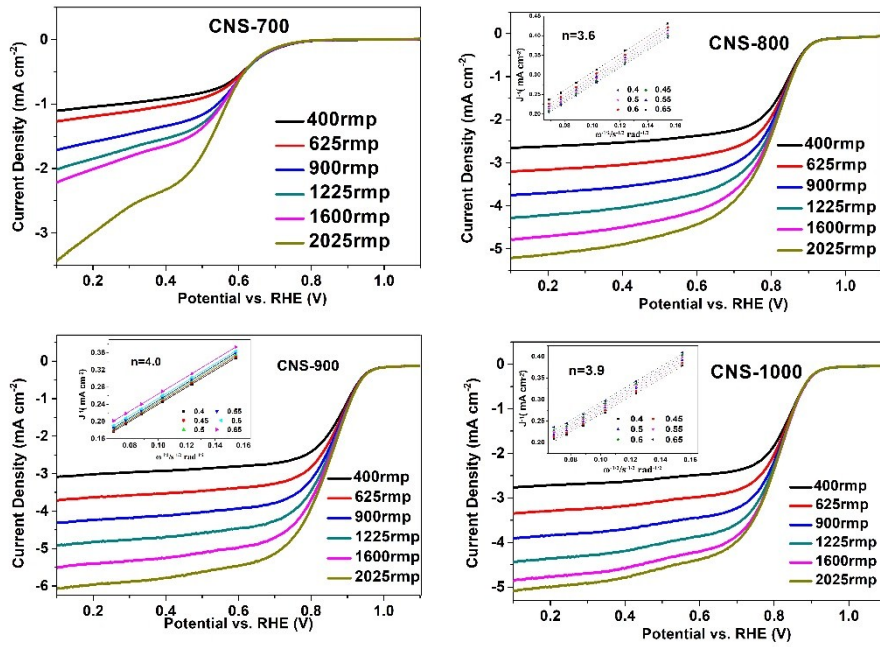


Figure S9 ORR polarization curves of CNS-700, CNS-800, CNS-900 and CNS-1000 at different rotation speeds

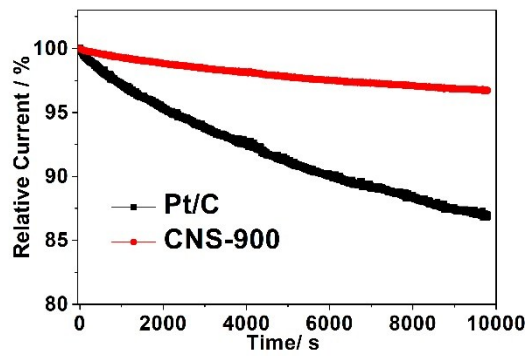


Figure S10 The i - t chronoamperometric responses of CNS-900 and Pt/C

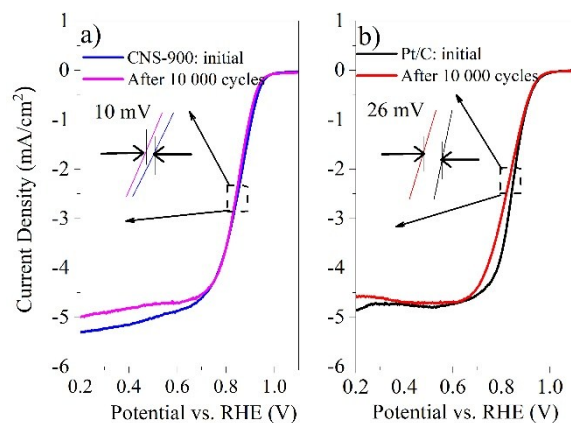


Figure S11 ORR polarization plots of CNS-900 (a) and Pt/C (b) before and after 10 000 potential cycles

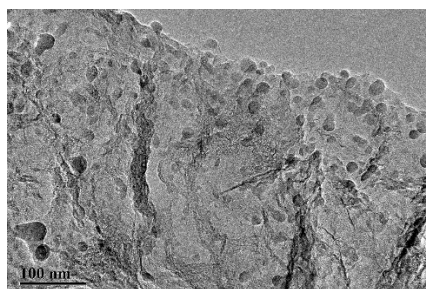


Figure S12 TEM image of CNS-900 after i-t chronoamperometric responses

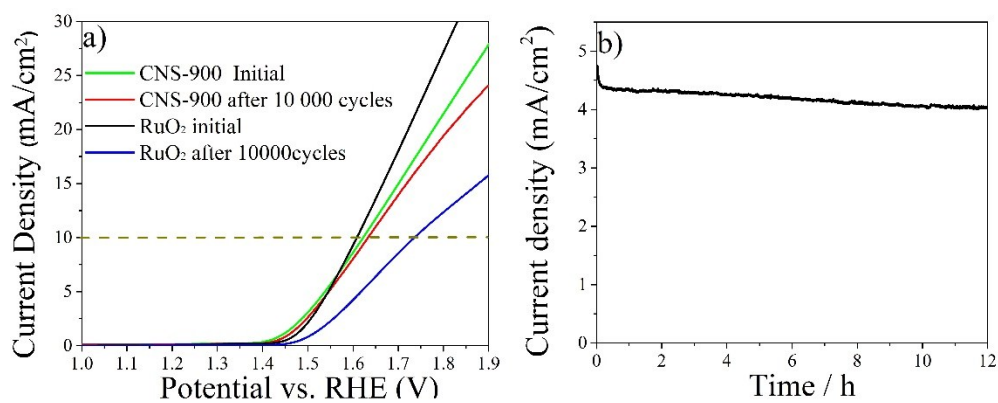


Figure S13 (a) LSV curves of the CNS-900 and RuO₂ catalyst before and after 10000 cycles; (b) Time-dependent current density of CNS-900 at an overpotential of 0.3 V for 12 h

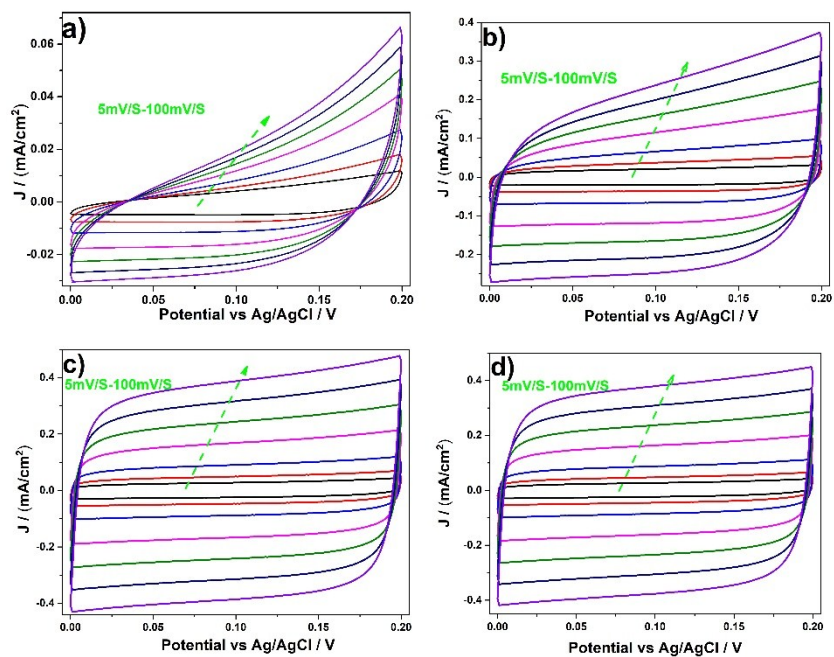


Figure S14 CV curves at 5-100 mV/s of (a) CNS-700 (b) CNS-800 (c) CNS-900 and (d) CNS-1000

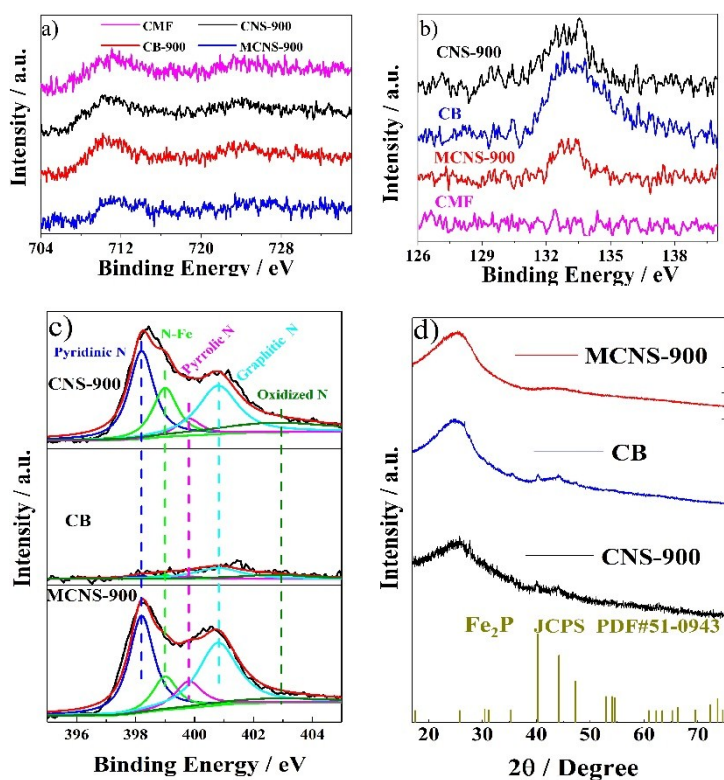


Figure S15 High-resolution (a) Fe 2p spectra, (b) P 2p spectra, and (c) N 1s spectra of CNS-900, CB, MCNS-900 and CMF catalysts; (d) XRD patterns of CNS-900, CB and MCNS-900

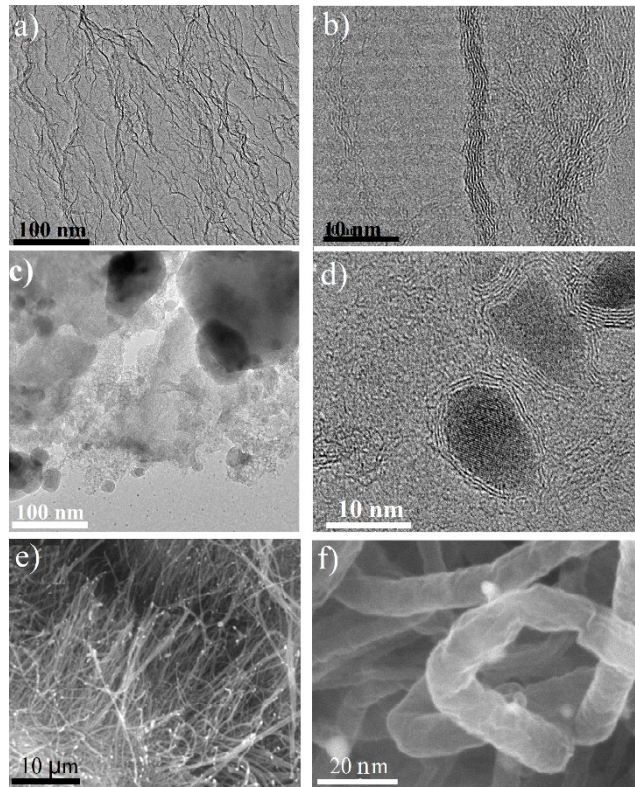


Figure S16 TEM images of MCNS-900(a, b) and CB(c, d); SEM images of CMF (e, f)

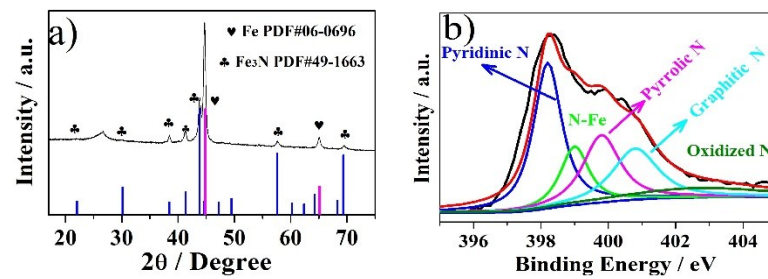


Figure S17 XRD patterns (a) and high-resolution N 1s spectra (b) of CMF sample

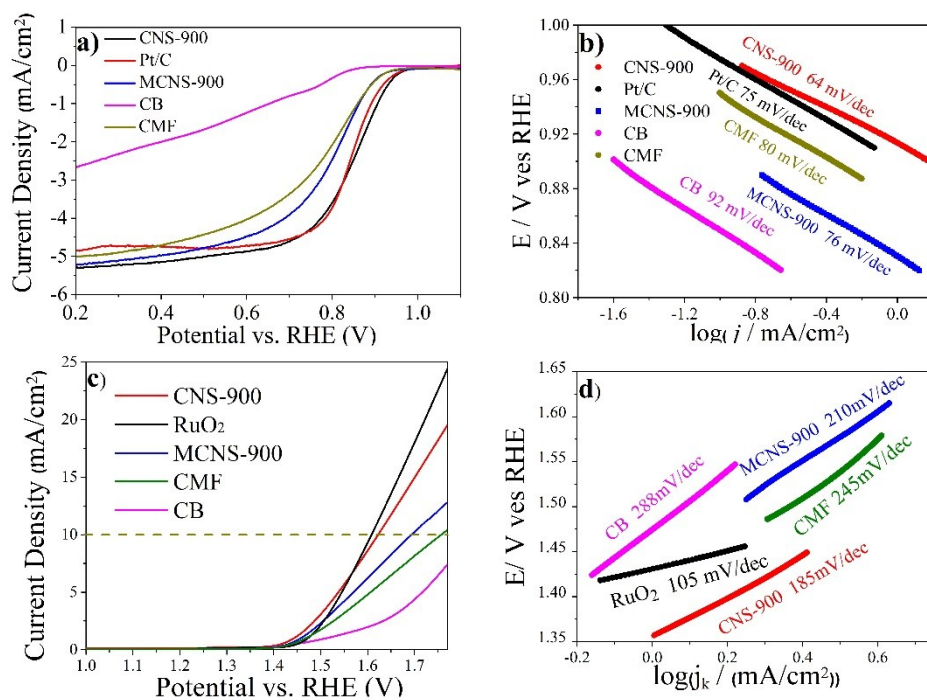


Figure S18 (a) ORR LSV curves of the CNS-900, MCNS-900, CB and Pt/C catalysts in O₂-saturated 0.1 M KOH with a rotation speed of 1600 rpm and a sweep rate of 10 mV/s; (b) Tafel slope values of CNS- 900, MCNS-900, CB and Pt/C for ORR; (c) OER LSV curves of the CNS-900, MCNS-900, CB and RuO₂ catalysts in Ar-saturated 0.1 M KOH with a rotation speed of 1600 rpm and a sweep rate of 10 mV/s; (d) Tafel slope values of CNS-900, MCNS-900, CB and RuO₂ for OER

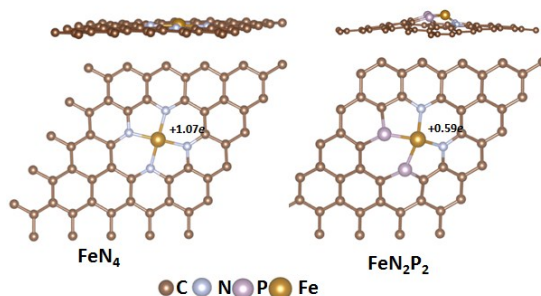


Figure S19 Top view and side view of the optimized FeN₄ and FeN₂P₂, respectively

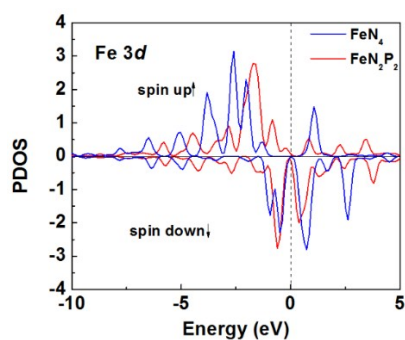


Figure S20 The PDOS profiles for FeN₄ and FeN₂P₂, respectively. The Fermi level is plotted with a black dotted line

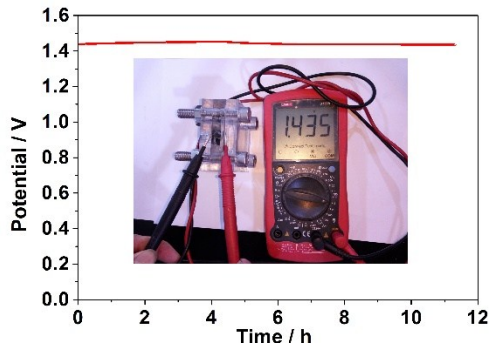


Figure S21 The open-circuit voltage test curve of the Zn-air battery with CNS-900 as cathode catalysts; the illustration is Photograph of the above Zn-air battery with an open-circuit voltage of 1.435 V

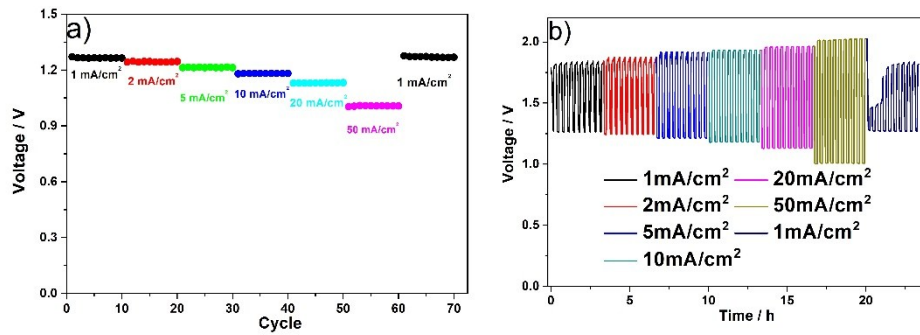


Figure S22 (a) Discharge voltage of the Zn-air battery using CNS-900 as the air-catalyst from 1-50 mA/cm²; (b) Discharge profiles of the Zn-air battery using CNS-900 the air-catalyst from low current density to high current density (1, 2, 5, 10, 20 and 50 mA/cm²)

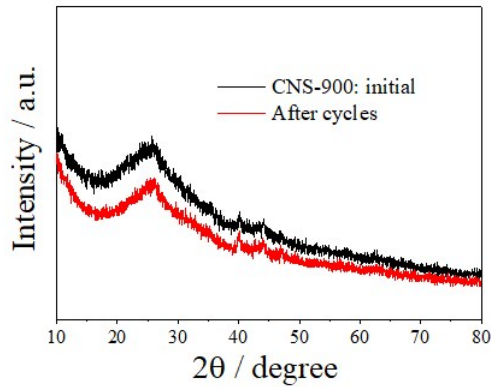


Figure S23 XRD patterns of CNS-900 catalysts initially and after the cycling test of rechargeable Zn-air batteries by using CNS-900 as a cathode

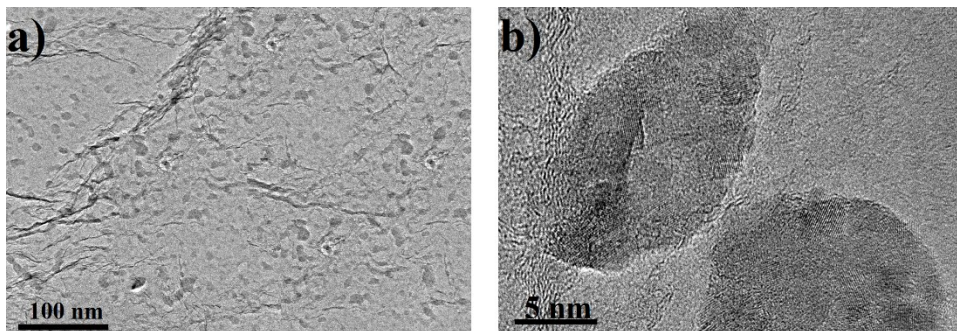


Figure S24 TEM of CNS-900 catalysts after the cycling test of rechargeable Zn-air batteries by using CNS-900 as a cathode

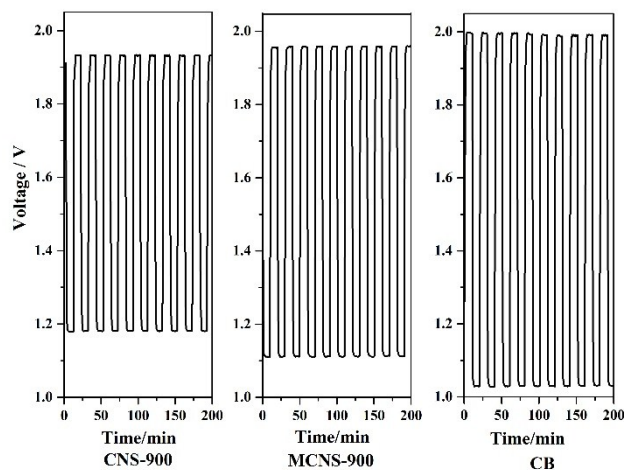


Figure S25 cyclic stability of CNS-900, MCNS-900 and CB based Zn-air battery at 10 mA/cm²

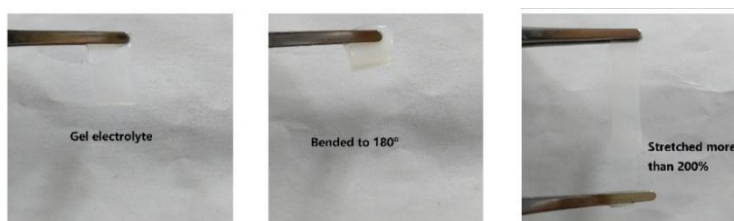


Figure S26 The morphology of the as-fabricated alkaline gel electrolyte, which is flexible, bendable, and stretchable



Figure S27 Photograph of all-flexible-solid-state rechargeable Zn-air battery with open circuit voltage at different angle

Table S1 Elemental composition and textural parameters of CNSs samples

	Elemental composition (wt %)						Textural parameters	
	N ^a	C ^a	H ^a	P ^a	Fe ^b	Fe ^c	S _{BET} (m ² /g)	V _{total} (cm ³ /g)
CMB	1.53	70.36	0.87	0.22	1.96	0.13	30.2	0.06
CB	1.13	75.21	0.65	0.41	2.53	0.24	98.5	0.13
CNS-700	23.67	45.70	1.37	0.29	2.67	0.32	158.2	0.40
CNS-800	12.56	52.90	1.10	0.30	2.92	0.30	189.4	0.58
CNS-900	10.24	66.44	0.80	0.66	3.09	0.25	215.5	0.90
CNS-1000	9.51	75.89	0.42	0.76	3.46	0.14	284.8	0.75

^aData were from elemental analysis. ^bData were from ICP. ^cData were from XPS.

Table S2 Content of N groups (wt %)

	Pyridinic N	Fe-N	Pyrrolic N	Graphitic N	Oxidized N
CNS-700	61.4	5.92	15.6	11.7	5.3
CNS-800	45.3	9.69	12.1	21.3	11.6
CNS-900	30.4	16.9	6.8	26.9	18.9
MCNS-900	34.2	12.8	10.4	31.2	11.5
CMF	34.6	13.9	20.8	19.4	11.1
CNS-1000	20.9	16.5	2.57	23.4	36.6
CB	8.6	6.3	6.5	50.1	28.4

Data were from XPS

Table S3 Comparative ORR parameters of onset potential, half potential and limiting current density

Catalyst	Onset potential (V vs. RHE)	Half potential (V vs. RHE)	Limiting current density (mA/cm ²)	Reference
CoNi/ carbon framework	0.91	0.80	4.1	8
Fe/Co-N/S doped carbon nanosheets	0.935	0.835	6.7	9
Co-NC@Al ₂ O ₃	0.91	0.86		10
NiFeS ₂ /S-GO	0.95	0.77	4.2	11
N, P, and S doped graphene-like carbon	0.96	0.857	5.7	12
NFe/CNs-700	0.937	0.863	5.4	13
Double-shelled NC@Co-NGC nanocages	0.92	0.82	5.0	14
Graphene Oxide/Carbon	0.88	0.7	5.4	15
Black/Amorphous Cobalt Borate				
B, N codoped nanocarbon	0.98	0.84	5.6	16
FeCo-N _x -carbon nanosheets	0.90	0.83	5.3	17
CoFe in N-doped CNTs with RGO	0.91	0.79	4.9	18
porous carbons with boron and Fe-N _x	0.968	0.838	5.4	19
FeNi and nitrogen-codoped carbons	0.98	0.83	4.8	20
CNS-900	0.976	0.844	5.4	This work

Table S4 Comparison of the bifunctional OER and ORR activity of CNS-900 with other electrocatalysts previously reported

Catalyst	$E_{1/2}$ (V vs. RHE)	$E_{j=10}$ (V vs. RHE)	ΔE ($E_{j=10}-E_{1/2}$)	Reference
CoNi/ carbon framework	0.80	1.60	0.80	8
Fe-Co in carbon matrix	0.79	1.67	0.88	18
FeNi-NC	0.83	1.64	0.81	20
3D Co-N-doped carbon spheres	0.86	1.72	0.86	21
Co-N _x -C in graphene	NA	NA	0.95	22
Ni ₃ Fe/N-C sheets	0.78	1.62	0.84	23
CuCo ₂ O ₄ /N-CNTs	-0.21 (SCE)	0.69 (SCE)	0.90	24
Nitrogen, phosphorus, and fluorine tri-doped graphene	0.73	1.72	0.99	25
N-Doped carbon nanosheets encapsulated Co ₉ S ₈	0.77	1.66	0.89	26
Nitrogen doped ultrathin carbon nanosheets	0.82	1.63	0.81	27
Cobalt and nitrogen co-doped hierarchically porous carbon	0.81	1.59	0.78	28
CNS-900	0.844	1.635	0.79	This work

References

1. G. Kresse and J. Hafner, *Physical Review B*, 1993, **47**, 558-561.
2. G. Kresse and J. Furthmuller, *Computational Materials Science*, 1996, **6**, 15-50.
3. P. E. Blochl, *Physical Review B*, 1994, **50**, 17953-17979.
4. G. Kresse and D. Joubert, *Physical Review B*, 1999, **59**, 1758-1775.
5. J. P. Perdew, K. Burke and M. Ernzerhof, *Physical Review Letters*, 1996, **77**, 3865-3868.
6. R. F. W. Bader, *Chemical Reviews*, 1991, **91**, 893-928.
7. G. Henkelman, A. Arnaldsson and H. Jónsson, *Computational Materials Science*, 2006, **36**, 354-360.
8. W. Wan, X. Liu, H. Li, X. Peng, D. Xi and J. Luo, *Applied Catalysis B: Environmental*, 2019, **240**, 193-200.
9. C. Li, H. Liu and Z. Yu, *Applied Catalysis B: Environmental*, 2019, **241**, 95-103.
10. L. Zhu, D. Zheng, Z. Wang, X. Zheng, P. Fang, J. Zhu, M. Yu, Y. Tong and X. Lu, *Advanced materials*, 2018, e1805268.
11. D. Zhou, Y. Jia, H. Yang, W. Xu, S. Kai, J. Zhang, S. Wang, Y. Kuang, B. Liu and X. Sun, *Journal of Materials Chemistry A*, 2018, **6**, 21162-21166.
12. X. Zheng, J. Wu, X. Cao, J. Abbott, C. Jin, H. Wang, P. Strasser, R. Yang, X. Chen and G. Wu, *Applied Catalysis B: Environmental*, 2019, **241**, 442-451.
13. S. Li, C. Cheng, H. W. Liang, X. Feng and A. Thomas, *Advanced materials*, 2017, **29**, 1700707.
14. S. Liu, Z. Wang, S. Zhou, F. Yu, M. Yu, C. Y. Chiang, W. Zhou, J. Zhao and J. Qiu, *Advanced materials*, 2017, **29**, 1700874.
15. J. Sun, D. Yang, S. Lowe, L. Zhang, Y. Wang, S. Zhao, P. Liu, Y. Wang, Z. Tang, H. Zhao and X.

- Yao, *Advanced Energy Materials*, 2018, **8**, 1801495.
16. T. Sun, J. Wang, C. Qiu, X. Ling, B. Tian, W. Chen and C. Su, *Advanced Science*, 2018, **5**, 1800036.
 17. S. Li, C. Cheng, X. Zhao, J. Schmidt and A. Thomas, *Angewandte Chemie International Edition*, 2018, **57**, 1856-1862.
 18. X. Liu, L. Wang, P. Yu, C. Tian, F. Sun, J. Ma, W. Li and H. Fu, *Angewandte Chemie International Edition*, 2018, **130**, 16398-16402.
 19. K. Yuan, S. Sfaelou, M. Qiu, D. Lützenkirchen-Hecht, X. Zhuang, Y. Chen, C. Yuan, X. Feng and U. Scherf, *ACS Energy Letters*, 2018, **3**, 252-260.
 20. L. Yang, X. Zeng, D. Wang and D. Cao, *Energy Storage Materials*, 2018, **12**, 277-283.
 21. S. Cai, Z. Meng, H. Tang, Y. Wang and P. Tsiakaras, *Applied Catalysis B: Environmental*, 2017, **217**, 477-484.
 22. C. Tang, B. Wang, H. F. Wang and Q. Zhang, *Advanced materials*, 2017, **29**, 1703185.
 23. G. Fu, Z. Cui, Y. Chen, Y. Li, Y. Tang and J. B. Goodenough, *Advanced Energy Materials*, 2017, **7**, 1601172.
 24. H. Cheng, M.-L. Li, C.-Y. Su, N. Li and Z.-Q. Liu, *Advanced Functional Materials*, 2017, **27**, 1701833.
 25. J. Zhang, L. Dai, *Angewandte Chemie International Edition* **2016**, 128, 13490-13494.
 26. L. Li, L. Song, H. Guo, W. Xia, C. Jiang, B. Gao, C. Wu, T. Wang, J. He, *Nanoscale* **2019**, 11, 901-907.
 27. H. Jiang, J. Gu, X. Zheng, M. Liu, X. Qiu, L. Wang, W. Li, Z. Chen, X. Ji, J. Li, *Energy & Environmental Science* **2019**, 12, 322-333.
 28. J. Sanetuntikul, S. Hyun, P. Ganesan, S. Shanmugam, *J. Mater. Chem. A* **2018**, 6, 24078-24085.